Journal of the Australian Ceramic Society (2020) 56:819–828
https://doi.org/10.1007/s41779-019-00403-w

RESEARCH

Synthesis and optical properties of $La_2O_2CO_3:Eu^{3+}$ hollow sphere phosphors by hydrothermal synthesis assisting with double-crucible carbonization method

Jinmiao Hou[1] · Yongting He[1] · Jingbao Lian[1,2] · Nianchu Wu[1,2] · Xue Zhang[1,2] · Jiao He[1,2]

Received: 9 January 2019 / Revised: 30 July 2019 / Accepted: 21 August 2019 / Published online: 2 September 2019

Abstract

Lanthanum oxide, europium oxide, hydrochloric acid, ammonia water, and carbon powder were used as the starting materials. Detailed characterizations were attained by X-ray diffraction (XRD), Fourier transform infrared spectroscopy (FT-IR), thermogravimetry/differential thermal analysis (TG-DTA), field emission scanning electron microscopy (FE-SEM), transmission electron microscopy (TEM), and photoluminescence (PL) spectroscopy. The $La(OH)_3$ precursor was synthesized by an hydrothermal synthesis method at 120 °C for 24 h, which was then converted into $La_2O_2CO_3$ phase through calcining the precursor at 800 °C for 2 h in a carbon atmosphere. It was demonstrated that the as-obtained $La_2O_2CO_3$ is a hollow sphere with uniform size about 200 nm. The formation mechanism of the $La_2O_2CO_3$ phase has also been proposed. Photoluminescence analysis showed that the $La_2O_2CO_3:Eu^{3+}$ phosphors have the strongest red emissions at 614 nm under 281 nm ultraviolet (UV) light excitation, which correspond to the $^5D_0 \rightarrow {}^7F_2$ transition of Eu^{3+} ions. The $La_2O_2CO_3:Eu^{3+}$ phosphors have double-exponential decay behavior and the calculated lifetime is determined to be $t_1 = 0.205$ μs and $t_2 = 1.177$ μs.

Keywords Lanthanum oxycarbonate · Hollow sphere · Hydrothermal synthesis · Double-crucible carbonization · Photoluminescence

Introduction

Lanthanide compounds are an attractive class of materials and have unique optical, catalytic, and magnetic properties, resulting from the unique configuration of unpaired 4*f* electrons and the rich structures of their energy levels [1–3]. Among them, lanthanum compounds have been widely studied in its hydroxide [4, 5], oxide [6], oxysulfide [7], oxysulfate [8], fluoride [9], oxyfluoride [10], oxychloride [11], carbonate [12], or oxycarbonate forms [13, 14], and these substances have been extensively applied in optoelectronic devices [15], phosphors [16, 17], solid electrolyte [8], catalytic [18], sorbent [19], gas sensor [20], and so on. Lanthanum oxycarbonate ($La_2O_2CO_3$), which is emerging as a kind of novel optical material, has been prepared into different microstructures and morphological assemblies [21]. It is known that many inorganic materials with different microstructures have various properties, even if they have the same chemical composition. For example, Ding et al. [22] presented a simple method to fabricate size-controlled $La_2O_2CO_3$ nanoparticles by annealing $La(OH)_3$ nanocrystallines in air atmosphere, which is printed on an interdigital electrode as a sensing material for CO_2 detection. Moreover, Chen et al. [23] prepared $La_2O_2CO_3$ nanorods with diameters of 13–15 nm and lengths of 100–150 nm by annealing the $La(OH)_3$ nanorods in a furnace at 400 °C for 2 h. It is shown that the sensor exhibits high gas response for CO_2 gas at an operating temperature of 325 °C, making it a potential candidate for practical detectors for CO_2 gas. Furthermore, Hou et al. [24] reported that they synthesized $La_2O_2CO_3$ samples with different morphologies (nanorod-shapes and nanoplate-shapes) at 500 °C for 2 h by an hydrothermal method and a precipitation method, respectively. They observed that one of the nanorod-shaped samples

✉ Jingbao Lian
lianjingbao@aliyun.com

[1] School of Mechanical Engineering, Liaoning Shihua University, Fushun 113001, People's Republic of China

[2] New Functional Materials Laboratory, Liaoning Shihua University, Fushun 113001, People's Republic of China

exhibited the best catalytic properties among the investigated samples in the oxidative coupling of methane (OCM) at low temperatures (420–500 °C). Therefore, the investigation of lanthanum oxycarbonate with controlled special structures and sizes would offer an opportunity to design these compounds as materials for specific applications.

As is known to us all, the hollow spherical structures possess low density, large surface area, stability, surface permeability, and well-aligned nanoporous structures, all of which make them attractive for scientific study. For instance, they might be used for nanoreactors, environmental applications, drug delivery, catalysts, batteries, supercapacitors, gas sensors, photoacoustic imaging, etc. Meanwhile, the hollow phosphors might radiate light more effectively than its counterpart due to their interior hollow structure. In many cases, however, the examples mentioned above are currently limited to mesoscale hollow spheres, that is, with sphere diameters exceeding 100 nm [25]. Various synthetic strategies have been developed for the preparation of such hollow structures including template and template-free methods, hydrothermal and solvothermal approaches, ultrasound, and microwave-assisted synthesis, ion-exchange synthesis, aerosol route, chemical vapor deposition, ostwald ripening, phase inversion, excimer laser ablation, and ultra-high voltage hard anodization [26–28]. However, to the best of our knowledge, there are few reports about $La_2O_2CO_3:Eu^{3+}$ hollow sphere phosphors by hydrothermal synthesis assisting with the double-crucible carbonization method.

In this regard, we focus on two aspects in this study. Firstly, hollow spherical $La_2O_2CO_3:Eu^{3+}$ phosphors were synthesized by the double-crucible carbonization of the $La(OH)_3:Eu^{3+}$ precursors which were prepared via a facile hydrothermal process. Secondly, phase structure, thermal conversion process, morphology, and optical properties of the products are discussed based on the results of XRD, FT-IR, TG-DTA, FE-SEM, TEM, UV-vis, and fluorescence spectroscopy analyses.

Experimental procedure

Sample preparation

Lanthanum oxide (La_2O_3, 99.99% purity), europium oxide (Eu_2O_3, 99.99% purity), hydrochloric acid (HCl, AR), ammonia water ($NH_3{\cdot}H_2O$, AR), and carbon powder (C, AR) were used as the starting materials. Rare earth oxide powders (La_2O_3, Eu_2O_3) were purchased from Jining Tianyi New Material Co. Ltd. China. The other reagents were purchased from Sinopharm Chemical Reagent Co. Ltd. Firstly, $LaCl_3$ solutions with La^{3+} ion concentration of 0.1 M was prepared by dissolving the corresponding La_2O_3 in dilute hydrochloric acid (HCl) solution. Secondly, $LaCl_3$ solution with volume of 60 mL was transferred to a 100-mL Teflon-lined stainless steel autoclave. Accompanied with stirring, ammonia water ($NH_3{\cdot}H_2O$) was added to $LaCl_3$ solution until a pH value of 7 was attained. The autoclaves were sealed and heated in an electric blast drying oven for hydrothermal synthesis at 120 °C for 24 h. After being naturally cooled to room temperature, the product was collected by filtering and cleaning with deionized water and absolute ethanol several times and then dried at 80 °C for 12 h in order to obtain the precursor. Finally, the precursor was calcined at 800 °C for 2 h in a carbon atmosphere by a double-crucible carbonization method in order to obtain the final product. The Eu^{3+} ion-doped target product was also synthesized using the same procedure. The doping molar concentration of Eu^{3+} ions was 9% in this study. The specific flow chart is shown in Fig. 1.

Sample characterization

Phase and structure analyses were conducted using X-ray powder diffraction (XRD) and Flourier transform infrared spectra (FT-IR) tools. The XRD pattern was operating at 40 kV and 30 mA with $CuK_\alpha = 0.15406$ nm using a D8 Advance X-ray diffractometer. Fourier transform infrared spectra (FT-IR) were recorded in the region of 4000–400 cm^{-1} using an Agilent Cary 660 FT-IR spectrophotometer by the KBr method. Thermogravimetry (TG) and differential thermal analysis (DTA) were performed using simultaneous differential thermal analysis and thermo-gravimetry (Q600 Simultaneous DSC-TGA). The absorption spectra were acquired on an Agilent Cary 5000 UV-visible spectrometer with barium sulphate as a reference. The particle morphologies of the products were observed by a Hitachi SU8010 field emission scanning electron microscope (FE-SEM) and a JEM-2100F transmission electron microscope (TEM). Photoluminescence (PL) spectra and decay times were measured using a Hitachi F-7000 fluorescence spectrophotometer equipped with IBH TemPro fluorescence lifetime measurement system.

Results and discussion

Phase and structure analysis

Figure 2 shows the XRD patterns of the precursor, the product calcined in a carbon atmosphere, as well as their corresponding standard JCPDS cards. It can be seen from Fig. 2a, that the precursor sample exhibits sharp diffraction peaks, which match the hexagonal lanthanum hydroxide phase ($La(OH)_3$, JCPDS-00-036-1481) without any impurity peaks, as shown in Fig. 2b. The chemical reactions in the formation of the precursor can be expressed as follows:

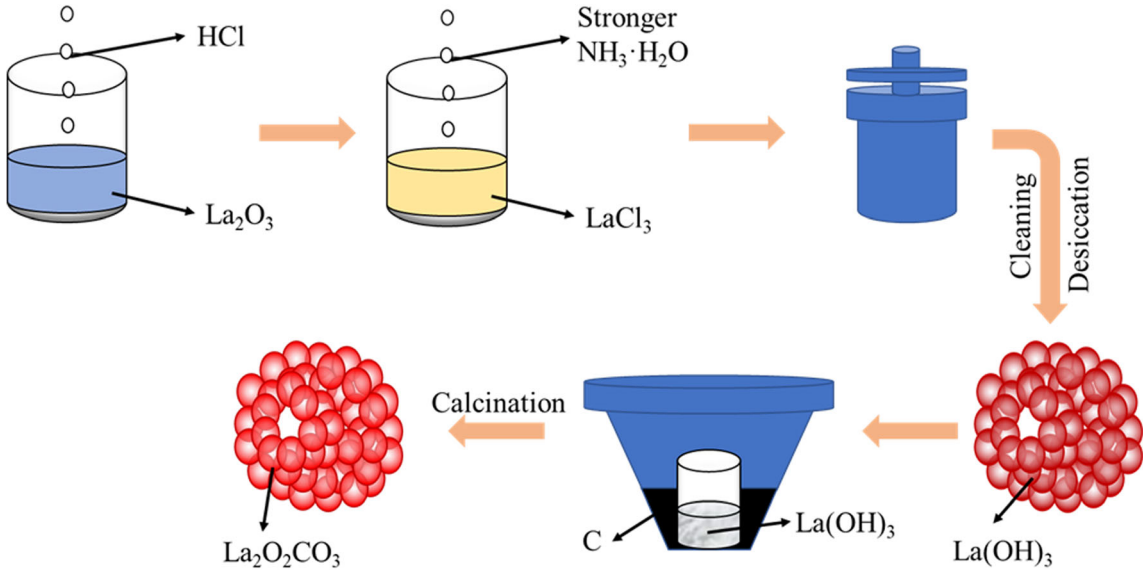

Fig. 1 Schematic illustration for the fabrication process of $La_2O_2CO_3$

$$La_2O_3 + 6HCl \rightleftharpoons LaCl_3 + 3H_2O \quad (1)$$

$$LaCl_3 \rightleftharpoons La^{3+} + 3Cl^- \quad (2)$$

$$NH_3 \cdot H_2O \rightleftharpoons NH_4^+ + OH^- \quad (3)$$

$$La^{3+} + 3OH^- \rightleftharpoons La(OH)_3\downarrow \quad (4)$$

After the precursor was calcined at 800 °C for 2 h in a carbon atmosphere, the characteristic diffraction peaks of the sample (Fig. 2c) are basically indexed to the hexagonal phase of $La_2O_2CO_3$ (JCPDS-01-084-1963), as shown in Fig. 2d. No $La(OH)_3$ or La_2O_3 phases were identified, revealing that the as-synthesized product is mainly composed of $La_2O_2CO_3$ phase, corresponding to the following chemical reaction:

$$2La(OH)_3 + 2C + O_2 \rightleftharpoons La_2O_2CO_3 + 3H_2O \quad (5)$$

Fourier transform infrared spectroscopy (FT-IR) was usually employed as an additional probe to evidence the presence of OH^- groups, CO_3^{2-} groups, as well as other inorganic species. The FT-IR spectra of the $La(OH)_3$ and the $La_2O_2CO_3$ in the range 4000–400 cm^{-1} are shown in Fig. 3. As can be seen from Fig. 3a, the IR absorption bands at 3612 cm^{-1}, 3430 cm^{-1}, 1630 cm^{-1}, and 650 cm^{-1} were associated with the OH stretching vibration and La-OH bending modes in lanthanum hydroxide. The bands at 1486 cm^{-1} and 1382 cm^{-1} are assigned to the C-O stretching vibration due to containing a small amount of CO_2. The result indicated that the $La(OH)_3$ has a high capacity for adsorbing CO_2. As can be seen from Fig. 3b, the absorption bands at 3630 cm^{-1} and 1630 cm^{-1} were associated with the water molecule vibration, indicating the existence of absorbed water in the $La_2O_2CO_3$. The bands between 1518 and 1362 cm^{-1} in the spectra of the $La_2O_2CO_3$ reveal the existence of carbonate groups, originating from the reaction of the $La(OH)_3$ with carbon dioxide (CO_2) in the carbon atmosphere. In addition, the two main vibration peaks of the $La_2O_2CO_3$ sample at 1085 cm^{-1} and 856 cm^{-1} were attributed to the υ_2 and υ_1 modes of the $La_2O_2CO_3$ [29]. The peak at 500 cm^{-1} was ascribed to the La-O stretching frequencies of the $La_2O_2CO_3$ [30]. These arguments are supported by the XRD results.

Thermal conversion process

To analyze the thermal conversion process of the precursor $La(OH)_3$ and the mixed sample ($La(OH)_3$ + C), TG and DTA measurements were carried out under a flowing air atmosphere. As shown in Fig. 4, the changes in the precursor ($La(OH)_3$) at elevated temperatures can be summarized as two steps: the first step occurred at the temperature region ranging from room temperature to ~ 350 °C. The weight loss of 11% at ~ 350 °C is likely due to the removal of hydration water in the chemical formula. According to the DTA trace, the endothermic peak centered at 340 °C indicates the process related with dehydration of the $La(OH)_3$, corresponding to the following reaction:

$$La(OH)_3 \rightleftharpoons La_2O_3 + 3H_2O\uparrow \quad (6)$$

At the second step, the weight was almost unchanged at ~ 350 to 800 °C, indicating La_2O_3 is stable. The changes in the mixed sample at elevated temperature can be summarized as four steps: the first step occurred at a temperature region ranging from room temperature to ~ 70 °C; the second step occurred at ~ 70 to 280 °C; the third step occurred at ~ 280 to ~

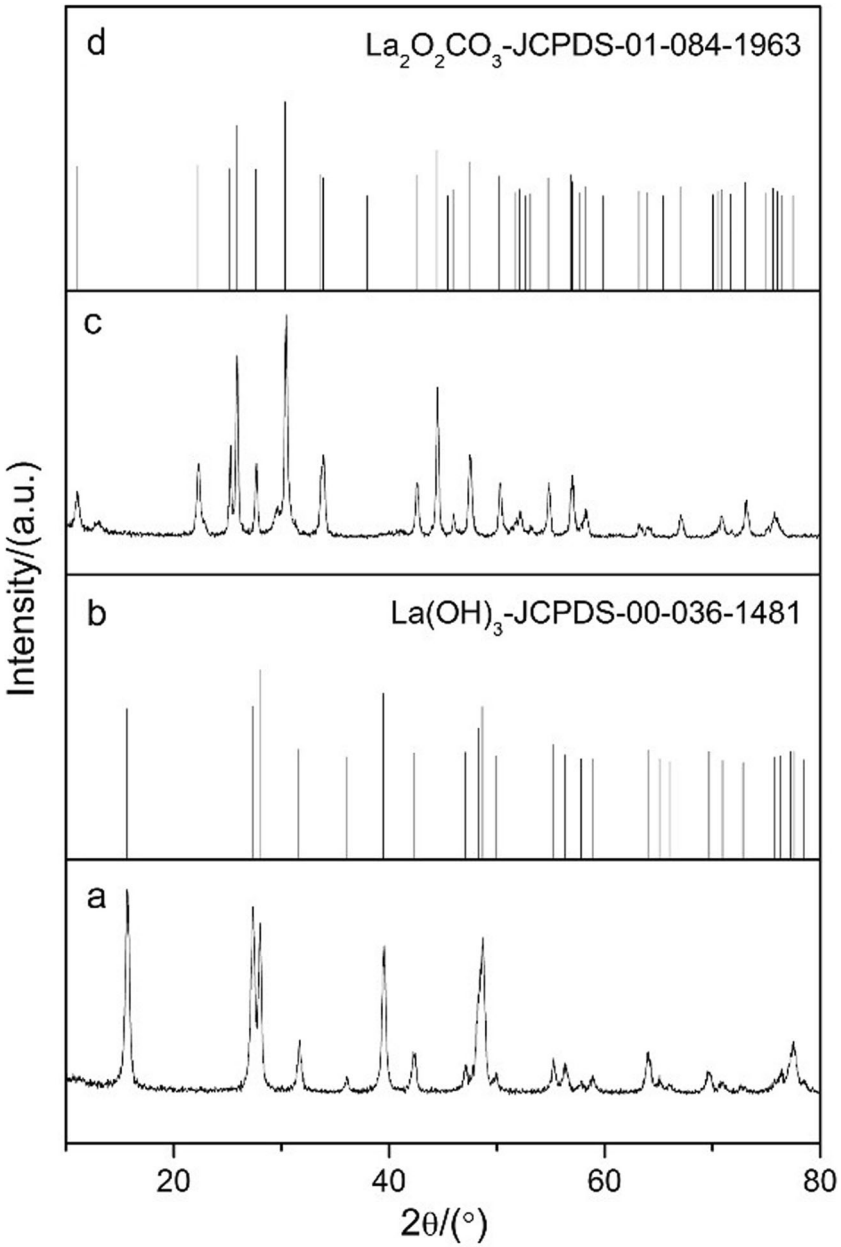

Fig. 2 XRD pattern of the $La(OH)_3$ and the $La_2O_2CO_3$

515 °C; and the last step occurred at ~ 515 to 800 °C. The first weight loss of 10% was attributed to the evaporation of water absorbed on to the surface of the mixed sample. Accordingly, this weight loss corresponds to a very weak endothermic peak at around 54 °C in the DTA curve. The second step, the weight was almost unchanged in the TG curve. The third step weight loss of 52.46% is likely due to two reasons. On the one hand, the process was related with the dehydration of the $La(OH)_3$, which is consistent with the thermal decomposition process of the $La(OH)_3$ analyzed above. On the other hand, the weight loss was attributed to the oxidation of carbon powder, and accompanied with carbon powder reacting with oxygen in the container to form CO_2. Furthermore, the $La(OH)_3$ was dehydrated to produce La_2O_3, which continues to react with CO_2 to form the $La_2O_2CO_3$ as evidenced, according to the DTA trace, by the broad exothermic peak centered at 480 °C. In the last step, the weight was almost unchanged, indicating $La_2O_2CO_3$ is stable at ~ 515 to 800 °C. These arguments are supported by the XRD and FT-IR results.

Morphology analysis

FE-SEM images of the $La(OH)_3$ and the $La_2O_2CO_3$ samples are shown in Fig. 5. The $La(OH)_3$ sample appears to be an aggregate on a large scale, quasi-spherical in shape, and the average size is about 1~2 μm in diameter (Fig. 5a). As can be seen from Fig. 5b, the morphology (shape, size distribution, and dispersity) of the $La_2O_2CO_3$ sample was similar to that of

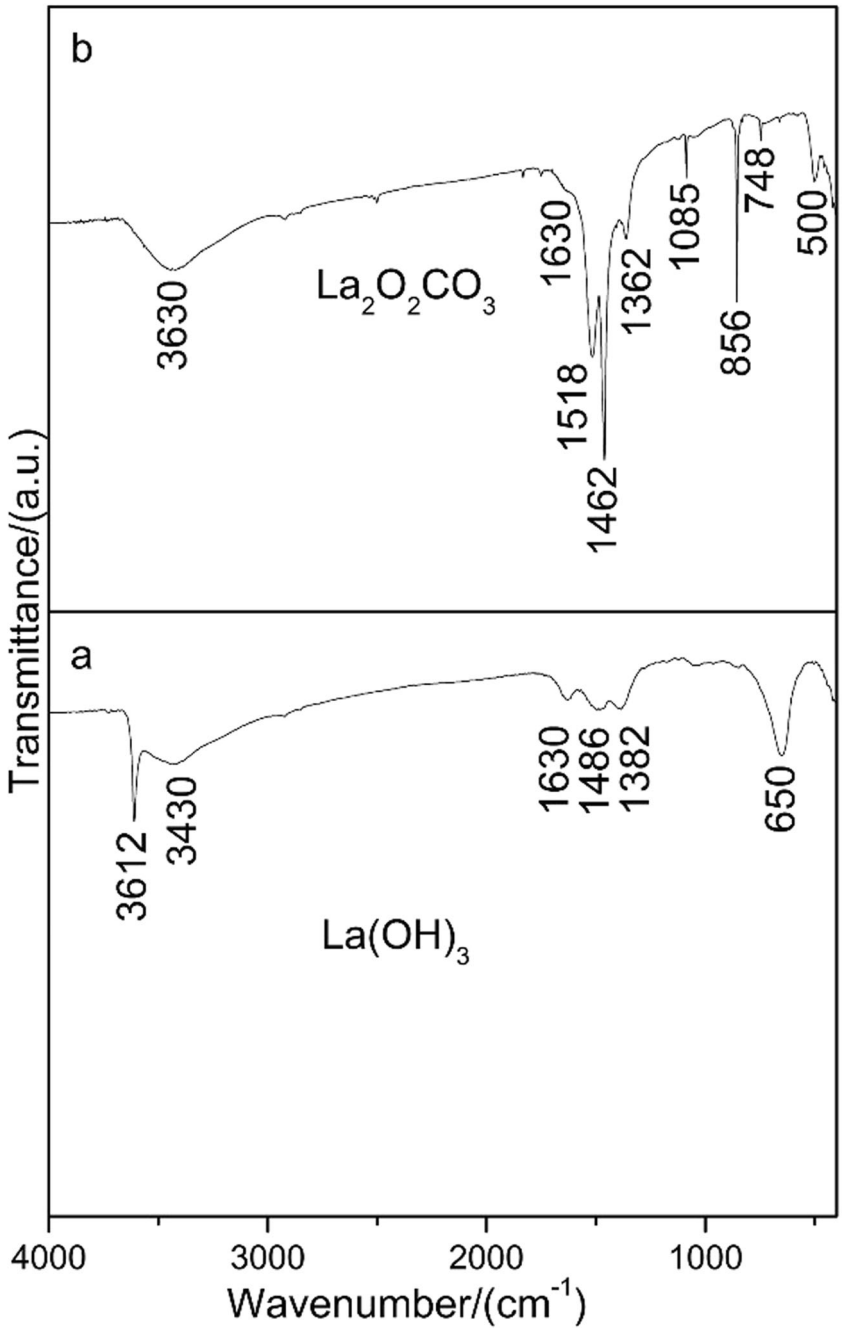

Fig. 3 FT-IR spectra of the $La(OH)_3$ samples and the calcined $La_2O_2CO_3$ samples

the $La(OH)_3$ sample. However, the $La_2O_2CO_3$ particle is more concentrated than the $La(OH)_3$ due to the high temperature carbonization process.

To clarify the hollow structure of the two samples, the morphology was further characterized by a TEM test. In Fig. 6 are shown TEM images of the $La(OH)_3$ and the $La_2O_2CO_3$ samples. Interestingly, it can be seen from Fig. 6a that the $La(OH)_3$ sample possesses a hollow sphere structure with a diameter of ~ 200 nm and a shell thickness of about 80 nm. Figure 6b gives a TEM image of the $La_2O_2CO_3$ and exhibits structure information. Careful observation shows that the carbonized sample still remains hollow structure and inheriting the shape of its $La(OH)_3$ precursor. Such a fascinating morphology was seldom seen before in the $La_2O_2CO_3$ material. Based on the above experimental results, a possible mechanism for the formation of the hollow spheres was proposed as follows: Initially, numerous tiny nuclei were formed in the hydrothermal reaction system, and the growth of the nucleus lead to the formation of nanoparticles. Then, for the minimization of surface energy, a great deal of nanoparticles tends to aggregate and assemble into a quasi-spherical structure with increasing hydrothermal time. Finally, the

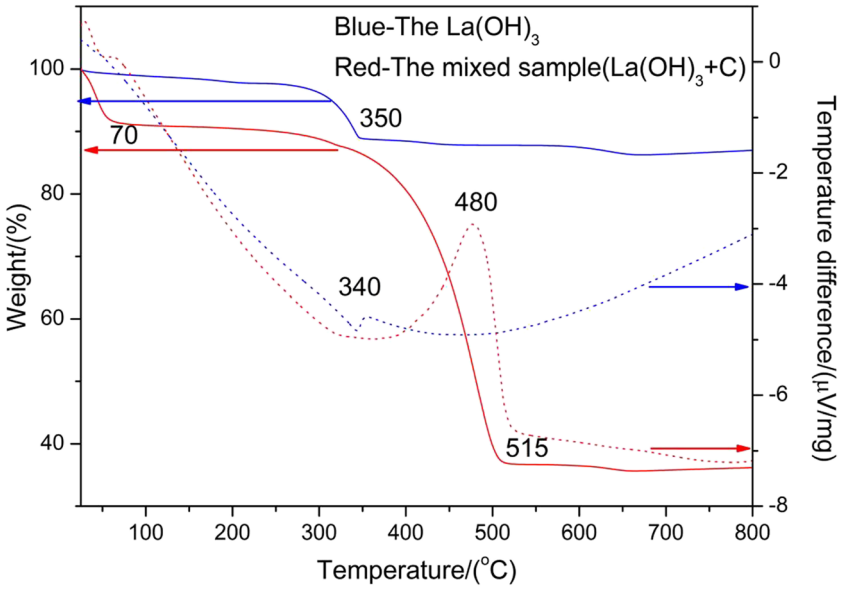

Fig. 4 TG-DTA curves of the $La(OH)_3$ and the mixed sample of $La(OH)_3$ and carbon powder: the full and dotted curves represent TG and DTA curves, respectively

carbonized samples also maintained their parents' morphologies and the change in the size is very slight.

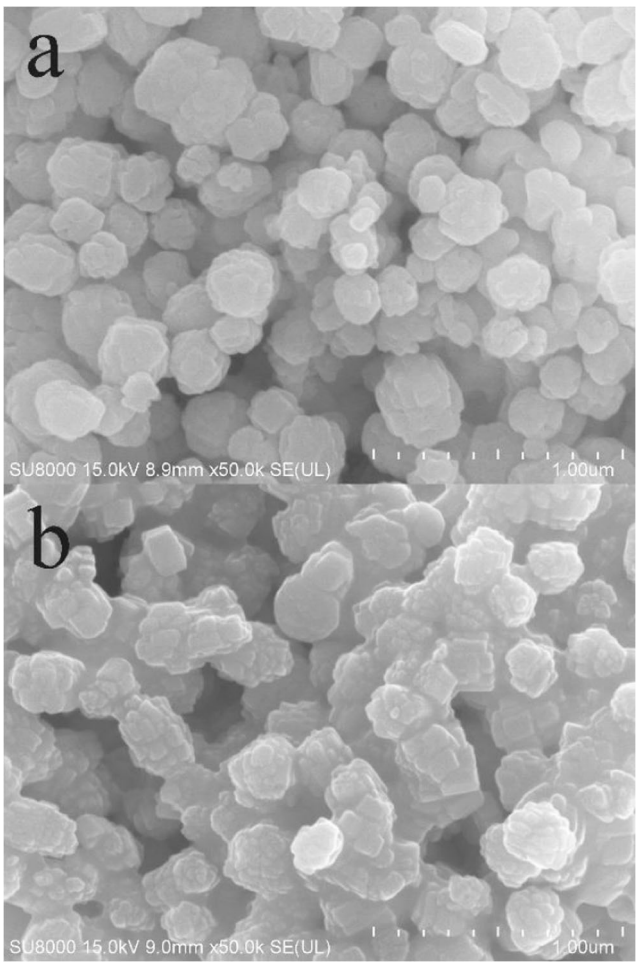

Fig. 5 FE-SEM images of **a** the precursor $La(OH)_3$ and **b** the $La_2O_2CO_3$ samples

Optical properties

UV-vis spectroscopy was used to characterize the optical absorbance of the $La(OH)_3$ and $La_2O_2CO_3$ hollow spheres. The absorption spectra were carried out to resolve the interband

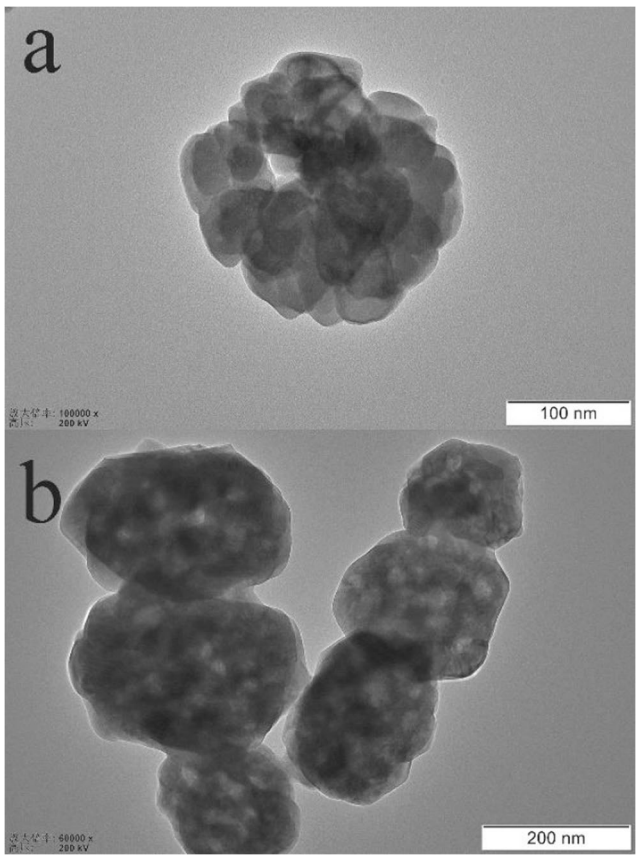

Fig. 6 TEM images of **a** the precursor $La(OH)_3$ and **b** the $La_2O_2CO_3$ samples

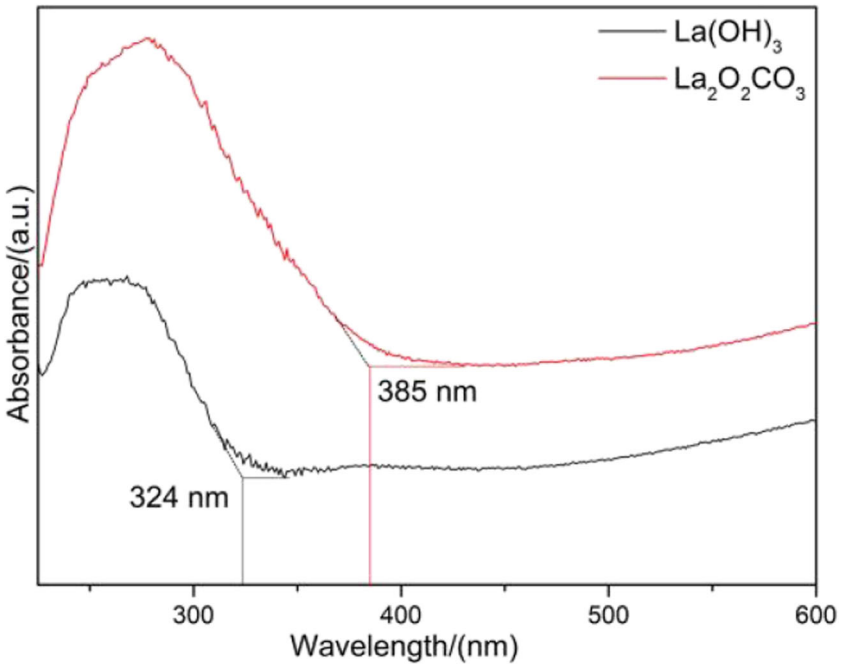

Fig. 7 The absorption spectra of the $La(OH)_3$ and the $La_2O_2CO_3$ samples

(valence-conduction band) transition, which allows us to calculate the band gap. The UV-vis absorption band edges located at 324 nm and 385 nm (see the slope in Fig. 7), respectively. It is well known that the optical band gap and absorption wavelength of a semiconductor have a characteristic relation:

$$E_g = 1240/\lambda \text{ (eV)} \quad (7)$$

in which E_g is the optical band gap and λ is the wave length of the photon (nm). Therefore, the E_g values of the $La(OH)_3$ and the $La_2O_2CO_3$ hollow spheres can be obtained by the extrapolation of the above relation to be 3.83 eV and 3.22 eV, respectively. This UV-vis spectroscopy shows characteristic band maxima at 260 nm and 280 nm for the $La(OH)_3$ and the $La_2O_2CO_3$ hollow spheres, respectively. The $La_2O_2CO_3$ has a wider and higher absorption band than the $La(OH)_3$, which is helpful for improving light absorption of the $La_2O_2CO_3$ hollow sphere.

Figure 8 presents the PL excitation and emission spectra of the $La(OH)_3:Eu^{3+}$ and the $La_2O_2CO_3:Eu^{3+}$ phosphors. As shown in Fig. 8a, the excitation spectra of the two phosphors are mainly composed of two excitation peaks located at 248 nm and 281 nm, respectively, which is due to the charge transfer transitions from the 2*p* orbital of the O^{2-} ions to the 4*f* orbital of the Eu^{3+} ions [31]. This result is consistent with the above UV-vis spectra. Moreover, two weak peaks centered at 394 nm and 464 nm are assigned to the $^7F_0 \rightarrow {}^5L_6$ and the

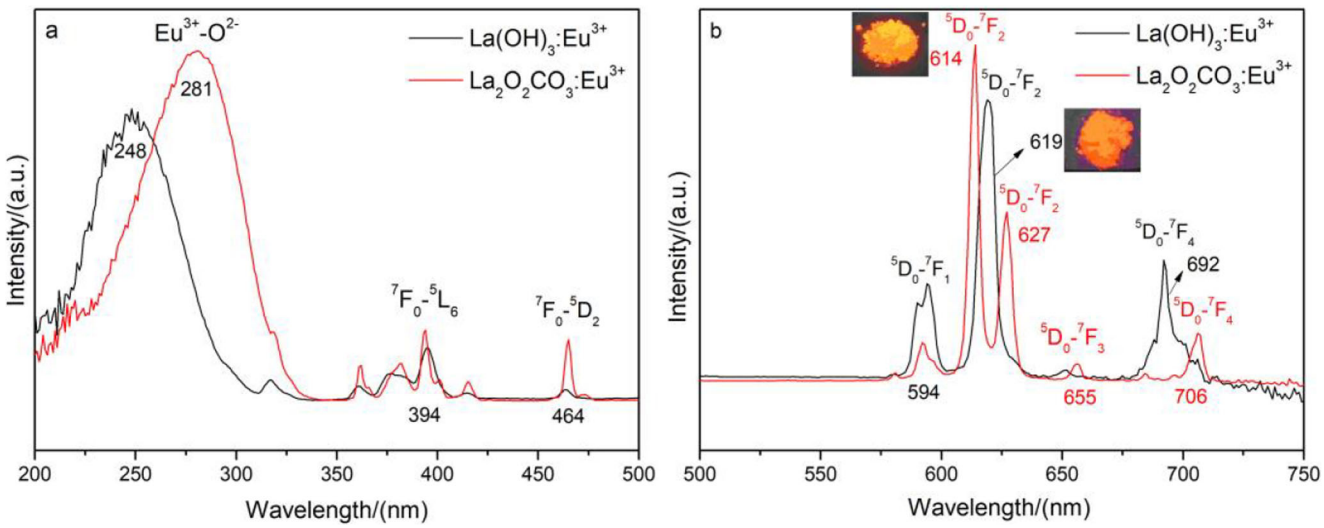

Fig. 8 PL excitation and emission spectra of the $La(OH)_3:Eu^{3+}$ and the $La_2O_2CO_3:Eu^{3+}$ phosphors. The inset of **b** is the $La(OH)_3:Eu^{3+}$ and the $La_2O_2CO_3:Eu^{3+}$ luminous photographs under 254 nm UV lamp

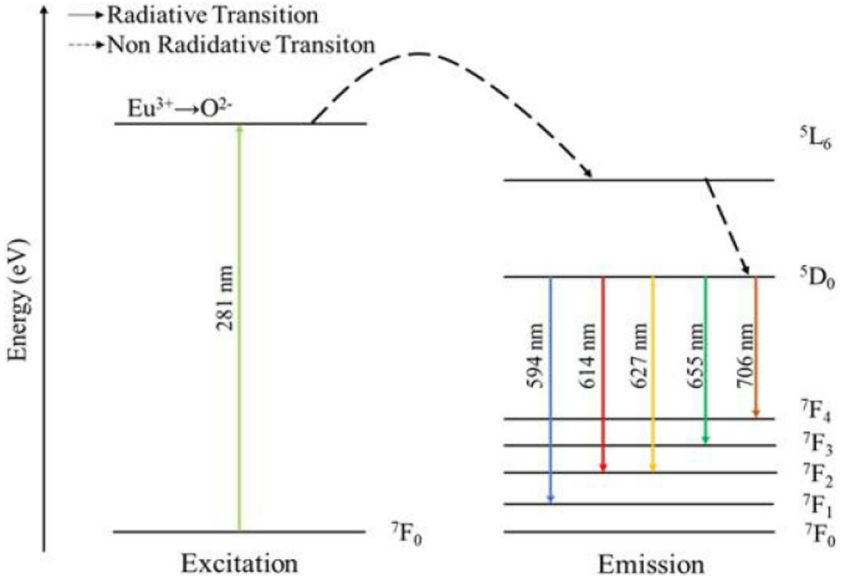

Fig. 9 The proposed possible energy mechanism of the Eu^{3+} ion-doped $La_2O_2CO_3$ phosphor. The position of the ground $^7F_0$ states of ions is assumed to be zero

$^7F_0 \rightarrow {}^5D_2$ transition of the Eu^{3+}, respectively. Upon excitation with 248 nm UV light, the $La(OH)_3:Eu^{3+}$ phosphor shows the corresponding emission spectrum consisting of the characteristic transitions of Eu^{3+}, i.e., $^5D_0 \rightarrow {}^7F_1$ (594 nm), $^5D_0 \rightarrow {}^7F_2$ (619 nm) and $^5D_0 \rightarrow {}^7F_4$ (692 nm), and the strongest one is located at 619 nm ($^5D_0 \rightarrow {}^7F_2$). Furthermore, upon excitation with 281 nm UV light, the $La_2O_2CO_3:Eu^{3+}$ phosphor shows a strong bright-red luminescence and the corresponding emission spectrum consists of the characteristic transitions of Eu^{3+}, i.e., $^5D_0 \rightarrow {}^7F_1$ (594 nm), $^5D_0 \rightarrow {}^7F_2$ (614 nm, 627 nm), $^5D_0 \rightarrow {}^7F_3$ (655 nm), and $^5D_0 \rightarrow {}^7F_4$ (706 nm). The strongest one is located at 614 nm, ascribed to the $^5D_0 \rightarrow {}^7F_2$ of the Eu^{3+} ion. The $^5D_0 \rightarrow {}^7F_2$ transition is symmetrically sensitive electric dipole transitions, and only the Eu^{3+} ion occurs when it is in a low symmetry position. On the basis of the above analyses, it can be clearly seen that there are two great differences in the PL spectra of the $La(OH)_3:Eu^{3+}$ and the $La_2O_2CO_3:Eu^{3+}$ phosphors, as follows: First, the excitation band of the $La(OH)_3:Eu^{3+}$ phosphor shifts 33 nm to a shorter-wavelength direction than that of the $La_2O_2CO_3:Eu^{3+}$ phosphor. The excitation spectra result reveals that the obvious redshift occurs from the $La(OH)_3:Eu^{3+}$ to the $La_2O_2CO_3:Eu^{3+}$ phosphors, and the position of the CTS bands

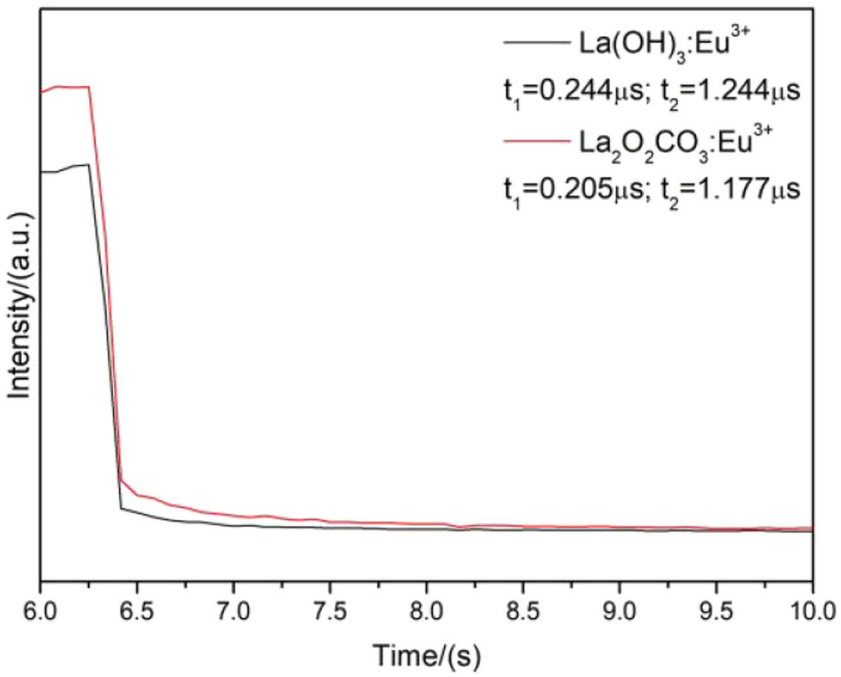

Fig. 10 The decay curves of the $La(OH)_3:Eu^{3+}$ and the $La_2O_2CO_3:Eu^{3+}$ phosphors

depends on the different host lattice. In addition, the excitation band intensity of the $La_2O_2CO_3$:Eu^{3+} phosphor is greater than that of the $La(OH)_3$:Eu^{3+} phosphor, indicating that the $La_2O_2CO_3$:Eu^{3+} phosphor possesses higher light absorption ability. Second, the $^5D_0 \rightarrow {}^7F_2$ transition intensity in the $La_2O_2CO_3$:Eu^{3+} phosphor is greatly enhanced in comparison with that in $La(OH)_3$:Eu^{3+} phosphor. These results reveal that the $La_2O_2CO_3$ is a better candidate host material than the $La(OH)_3$ for Eu^{3+} doping phosphor, as confirmed by the luminous photographs of the $La(OH)_3$:Eu^{3+} and the $La_2O_2CO_3$:Eu^{3+} phosphors under a 254 nm UV lamp (the inset of Fig. 8b). Based on the results of the luminescence spectrum, the following possible mechanism is proposed. The energy level diagram of Eu^{3+} ions in the $La_2O_2CO_3$ host lattice with all probable dipole transitions is shown in Fig. 9. As mentioned above, the $La_2O_2CO_3$:Eu^{3+} phosphors show intense luminescence in the visible light region. The intense luminescence of Eu^{3+} originates from an efficient energy transfer from the O^{2-} state to the Eu^{3+}energy state and then the electrons are expected to excite to the $^5L_6$ state, which decays nonradiatively to the $^5D_0$ state followed by radiative decay to lower levels of ^7F_J (J = 1–4) [32]. This is the origin of the luminescence processes of the Eu^{3+} ion in the visible light region.

Figure 10 shows the decay curves of the $La(OH)_3$:Eu^{3+} and the $La_2O_2CO_3$:Eu^{3+} phosphors excited by ultraviolet light at 248 nm and 281 nm, respectively. The luminescence life times for the strongest $^5D_0 \rightarrow {}^7F_2$ transitions of Eu^{3+} in the $La(OH)_3$ and the $La_2O_2CO_3$ hosts are shown in Fig. 10. The fluorescence decay curves can be well fitted by a double-exponential function as

$$I = I_0 + \mathrm{Aexp}(t/\tau_1) + \mathrm{Bexp}(t/\tau_2) \quad (8)$$

where I represents the decaying luminescence intensity, I_0 is the initial intensity, t the time, τ_1 and τ_2 are the decay time for the exponential components, respectively. The fitting results are shown inside Fig. 10. Two lifetimes, $\tau_1 = 0.244$ μs and $\tau_2 = 1.244$ μs have been obtained for the Eu^{3+} transition in $La(OH)_3$ host and two lifetimes, $\tau_1 = 0.205$ μs and $\tau_2 = 1.177$ μs also have been obtained for Eu^{3+} transition in $La_2O_2CO_3$ host. It can be seen from Fig. 10 that the fluorescence lifetime of $La_2O_2CO_3$:Eu^{3+} is almost the same as that of the $La(OH)_3$:Eu^{3+}. The result suggests that the $La_2O_2CO_3$:Eu^{3+} phosphor may have potential applications in the ultra-fast X-ray image field.

Conclusions

In summary, the $La_2O_2CO_3$:Eu^{3+} hollow sphere phosphors were successfully achieved by hydrothermal synthesis assisting with a double-crucible carbonization method. The present study shows that the precursor $La(OH)_3$ was synthesized by an hydrothermal synthesis method at 120 °C for 24 h, and $La_2O_2CO_3$ could be obtained by calcining the $La(OH)_3$ at 800 °C for 2 h in a carbon atmosphere. It was demonstrated that the obtained $La_2O_2CO_3$ has a hollow quasi-sphere structure and a typical size of about 200 nm in diameter. The strongest emission peak for the $La_2O_2CO_3$:Eu^{3+} bright-red phosphor was observed to be located at 614 nm under 281 nm UV light excitation, and this phosphor possesses double-exponential decay behavior, and the corresponding fluorescence lifetimes are $\tau_1 = 0.205$ μs and $\tau_2 = 1.177$ μs. These results suggest that the $La_2O_2CO_3$:Eu^{3+} hollow sphere may have potential applications in optoelectronic devices (fast X-ray imaging), catalytic, sorbent, and gas sensor fields.

Funding information This work was supported by National Students' Plaform for Innovation and Entrepreneurship Training Program (No.201810148015), the Nature Science Foundation of Liaoning Province of China (No. 20170540582), and the National Natural Science Foundation of China (No. 51701090).

References

1. Sun, C., Xue, D.: Perspectives of multiscale rare earth crystal materials. CrystEngComm. **21**, 1838–1852 (2019)
2. Patel, K., Zhang, J., Ren, S.: Rare-earth-free high energy product manganese-based magnetic materials. Nanoscale. **10**, 11701–11718 (2018)
3. Kaczmarek, A., Van Hecke, K., Van Deun, R.: Nano- and microsized rare-earth carbonates and their use as precursors and sacrificial templates for the synthesis of new innovative materials. Chem Soc Rev. **44**, 2032–2059 (2015)
4. Sun, C., Carpenter, C., Pratx, G., Xing, L.: Facile synthesis of amine-functionalized Eu^{3+}-doped $La(OH)_3$ nanophosphors for bioimaging. Nanoscale Res Lett. **6**, 24 (2011)
5. Hu, C., Liu, H., Dong, W., Zhang, Y., Bao, G., Lao, C., Wang, Z.: $La(OH)_3$ and La_2O_3 nanobelts-synthesis and physical properties. Adv Mater. **19**, 470–474 (2007)
6. Liu, J., Wang, G., Lu, L., Guo, Y., Yang, L.: Facile shape-controlled synthesis of lanthanum oxide with different hierarchical micro/nanostructures for antibacterial activity based on phosphate removal. RSC Adv. **7**, 40965–40972 (2017)
7. Balda, R., Hakmeh, N., Barredo-Zuriarrain, M., Merdrignac-Conanec, O., García-Revilla, S., Arriandiaga, M., Fernández, J.: Influence of upconversion processes in the optically-induced inhomogeneous thermal behavior of erbium-doped lanthanum oxysulfide powders. Materials. **9**, 353 (2016)
8. Yamamoto, S., Tamura, S., Imanaka, N.: New type of potassium ion conducting solid based on lanthanum oxysulfate. J Alloys Compd. **418**, 226–229 (2006)
9. Wang, M., Jiang, G., Tang, Y., Shi, Y.: LaF_3 and LaF_3:Ln^{3+} (Ln = Eu, Tb) hierarchical microstructures: synthesis, characterization and photoluminescence. CrystEngComm. **15**, 1001–1006 (2013)
10. Rodrigues, E., Souza, E., Monteiro, J., Gaspar, R., Mazali, I., Sigoli, F.: Non-stabilized europium-doped lanthanum oxyfluoride and fluoride nanoparticles well dispersed in thin silica films. J Mater Chem. **22**, 24109–24123 (2012)
11. Kim, D., Jang, J., Ahn, S., Kim, S., Park, J.: Novel blue-emitting Eu^{2+}-activated LaOCl:Eu materials. J Mater Chem C. **2**, 2799–2805 (2014)

12. Jeevanandam, P., Koltypin, Y., Palchik, O., Gedanken, A.: Synthesis of morphologically controlled lanthanum carbonate particles using ultrasound irradiation. J Mater Chem. **11**, 869–873 (2011)
13. Shahraki, S., Shiri, F., Beyzaei, H., Khosravi, F.: Synthesis, characterization, protein interaction and antibacterial activity of a lanthanum(III) complex $[La(Trp)_3(OH_2)_2]$ (Trp=tryptophan) as a new precursor for synthesis of $La_2O_2CO_3$ nanoparticles. New J Chem. **41**, 8413–8421 (2017)
14. Mu, Q., Wang, Y.: Synthesis, characterization, shape-preserved transformation, and optical properties of $La(OH)_3$, $La_2O_2CO_3$, and La_2O_3 nanorods. J Alloys Compd. **509**(2), 396–401 (2011)
15. Pavunny, S., Scott, J., Katiyar, R.: Lanthanum gadolinium oxide: a new electronic device material for CMOS logic and memory devices. Materials. **7**, 2669–2696 (2014)
16. Masui, T., Koyabu, K., Tamura, S., Imanaka, N.: Synthesis of a new green-emitting phosphor based on lanthanum oxycarbonate ($La_2O_2CO_3$-II). J Mater Sci. **40**, 4121–4123 (2005)
17. Manashirov, O., Zvereva, E., Lobanov, A.: A new lanthanum oxysulfide_based IR phosphor with a controlled luminescence decay time. Inorg Mater. **51**(5), 466–472 (2015)
18. Estruch Bosch, C., Copley, M., Eralp, T., Bilbe, E., Thybaut, J., Marin, G., Collier, P.: Tailoring the physical and catalytic properties of lanthanum oxycarbonate nanoparticles. Appl Catal A Gen. **536**(25), 104–112 (2017)
19. Li, X., Zhao, Z., Zeng, L., Zhao, J., Tian, H., Chen, S., Li, K., Sang, S., Gong, J.: On the role of Ce in CO_2 adsorption and activation over lanthanum species. Chem Sci. **9**, 3426–3437 (2018)
20. Haenscha, A., Koziejb, D., Niederbergerb, M., Barsana, N., Weimara, U.: Rare earth oxycarbonates as a material class for chemoresistive CO_2 gas sensors. Procedia Engineering. **5**, 139–142 (2010)
21. Zhao, D., Yang, Q., Han, Z., Zhou, J., Xu, S., Sun, F.: Biomolecule-assisted synthesis of rare earth hydroxycarbonates. Solid State Sci. **10**(1), 31–39 (2008)
22. Ding, D., Lu, W., Xiong, Y., Pan, X., Zhang, J., Ling, C., Du, Y., Xue, Q.: Facile synthesis of $La_2O_2CO_3$ nanoparticle films and its CO_2 sensing properties and mechanisms. Appl Surf Sci. **426**, 725–733 (2017)
23. Chen, G., Han, B., Deng, S., Wang, Y., Wang, Y.: Lanthanum dioxide carbonate $La_2O_2CO_3$ nanorods as a sensing material for chemoresistive CO_2 gas sensor. Electrochim Acta. **127**(5), 355–361 (2014)
24. Hou, Y., Han, W., Xia, W., Wan, H.: Structure sensitivity of $La_2O_2CO_3$ catalysts in the oxidative coupling of methane. ACS Catal. **5**(3), 1663–1674 (2015)
25. Leidinger, P., Popescu, R., Gerthsen, D., Feldmann, C.: Nanoscale $La(OH)_3$ hollow spheres and fine-tuning of its outer diameter and cavity size. Small. **6**(17), 1886–1891 (2010)
26. Zhao, D., Yang, Q., Han, Z., Sun, F., Tang, K., Yu, F.: Rare earth hydroxycarbonate materials with hierarchical structures: preparation and characterization, and catalytic activity of derived oxides. Solid State Sci. **10**(8), 1028–1036 (2008)
27. Niu, H., Min, Q., Tao, Z., Song, J., Mao, C., Zhang, S., Chen, Q.: One-pot facile synthesis and optical properties of porous $La_2O_2CO_3$ hollow microspheres. J Alloys Compd. **509**(3), 744–747 (2011)
28. Hou, F., Zhao, H., Song, H., Chou, L., Zhao, J., Yang, J., Yan, L.: Insight into the structure evolution and the associated catalytic behavior of highly dispersed Pt and PtSn catalysts supported on $La_2O_2CO_3$ nanorods. RSC Adv. **7**(77), 48649–48661 (2017)
29. Levan, T., Che, M., Tatibouet, J., Kermarec, M.: Infrared study of the formation and stability of $La_2O_2CO_3$ during the oxidative coupling of methane on La_2O_3. J Catal. **142**(1), 18–26 (1993)
30. Wang, F., Ta, N., Li, Y., Shen, W.: $La(OH)_3$ and $La_2O_2CO_3$ nanorod catalysts for Claisen-Schmidt condensation. Chin J Catal. **35**(3), 437–443 (2014)
31. Li, G., Peng, C., Zhang, C., Xu, Z., Shang, M., Yang, D., Kang, X., Wang, W., Li, C., Cheng, Z., Lin, J.: Eu^{3+}/Tb^{3+}-doped $La_2O_2CO_3$/La_2O_3 nano/microcrystals with multiform morphologies: facile synthesis, growth mechanism, and luminescence properties. Inorg Chem. **49**(22), 10522–10535 (2010)
32. Kaczmarek, A., Miermans, L., Deun, R.: Nano- and microsized Eu^{3+} and Tb^{3+}-doped lanthanide hydroxycarbonates and oxycarbonates. The influence of glucose and fructose as stabilizing ligands. Dalton Trans. **42**(13), 4639–4649 (2013)